EXPLORING LOW-RANK PROPERTY IN MULTIPLE INSTANCE LEARNING FOR WHOLE SLIDE IMAGE CLASSIFICATION

Anonymous authors
Paper under double-blind review

ABSTRACT

The classification of gigapixel-sized whole slide images (WSIs) with slide-level labels can be formulated as a multiple-instance-learning (MIL) problem. State-of-the-art models often consist of two decoupled parts: *local feature embedding* with a pre-trained model followed by a *global feature aggregation* network for classification. We leverage the properties of the apparent similarity in high-resolution WSIs, which essentially exhibit *low-rank* structures in the data manifold, to develop a novel MIL with a boost in both feature embedding and feature aggregation. For feature embedding, we extend the contrastive learning with a pathology-specific Low-Rank Constraint (LRC), allowing samples (i.e., patches) belonging to the same pathological tissue in the low-rank subspace are pulled together, while simultaneously pushing apart those from different latent subspace. At the feature aggregation stage, we highlight the importance of instance correlation modeling, but we refrain from directly using the transformer encoder considering the $O(n^2)$ complexity. We introduce an iterative low-rank attention MIL (ILRA-MIL) model to aggregate features with low-rank learnable latent vectors to model global interactions among all instances. ILRA-MIL with LRC pre-trained features achieves strong empirical results across diverse benchmarks, including (i) 96.49% AUC on the CAMELYON16 for binary metastasis classification , (ii) 97.63% AUC on the TCGA-NSCLC for lung cancer subtyping, and (iii) 0.6562 kappa on the large-scale PANDA dataset for prostate cancer classification. Code will be available.

1 INTRODUCTION

Recent artificial intelligence in digital pathology has presented the potential to analyze gigapixel whole-slide images (WSIs), but there are challenges that remain unsolved, including limited samples for training deep learning models and the extremely high resolution of WSI images Lu et al. (2021c); Campanella et al. (2019); Shao et al. (2021); Sharma et al. (2021); Lu et al. (2021b).

Since the relationship between input images and target labels is highly ill-posed, e.g., on CAMELYON16, 1.5 million 224×224 input image tiles against 270 WSI-level labels, one has to decompose the model into two separate stages, *local feature embedding* and *global feature aggregation*. Biological tissues in WSIs exhibit a wide variety of and there are still high semantic and background similarity among different image patches from the same type of tissue. One fundamental challenge is therefore to perform the feature embedding that faithfully captures only the relevant biological information and allows for quantitative comparison, categorization, and interpretation. After embedding, the standard MIL uses non-parametric max-/mean-pooling to perform slide-level classification. Such simplified schemes might lead to sub-optimal feature aggregation for WSI classification and the models are unable to learn correlations among instances due to the weak supervision signal.

As consistent with the findings in natural images Cong et al. (2013); Zhou et al. (2014); Zhang et al. (2013); Liu et al. (2012), we empirically find that gigapixel WSIs exhibit essentially low-rank property in the data manifold (see evidences in Appendix A). We aim to harness the low-rank property for WSI classification. The first intention is to learn a low-dimensional feature embedding in a discriminative way by extending contrastive loss with a low-rank constraint. For global feature aggregation, it would be beneficial for MIL to learn potential nonlinear interactions between instances, which

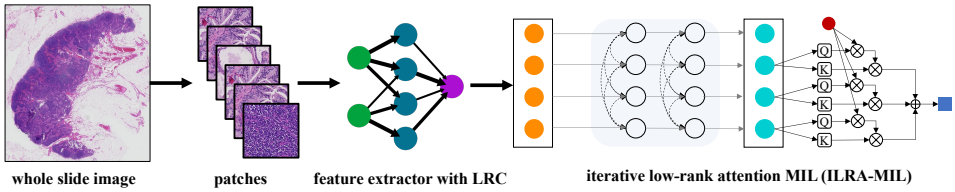

Figure 1: The proposed pipeline.

may help the model become more context-aware Lu et al. (2021c). To this end, we introduce self-attention with a low-rank matrix that forms an attention bottleneck with which all instances must interact, allowing it to handle large-scale bag sizes with a small computation overhead. It resolves the quadratic complexity $O(n^2)$ caused by the global self-attention.

Our main contributions: (i) We extend contrastive learning with a low-rank constraint (LRC) to learn feature embedding using unlabeled WSI data; (ii) We use iterative low-rank attention MIL (ILRA-MIL) to process a large bag of instances, allowing it to naturally encode cross-instance interactions; (iii) Extensive experiments on public benchmarks are conducted. Remarkably, ILRA-MIL improves over baselines including attention-pooling and transformer-based MIL by a large margin.

2 Related Work

2.1 Local Feature Embedding in MIL

Most methods conduct feature embedding with the ResNet50 pre-trained on ImageNet Lu et al. (2021c); Campanella et al. (2019). However, there is a significant domain deviation between pathological images and natural images, and this might lead to sub-optimal patch features for WSI classification. Contrastive learning paves a way for pathology-specific image pre-training Lu et al. (2019); Li et al. (2021); Chen et al. (2020a); Ciga et al. (2022); Stacke et al. (2021). The fundamental idea is to pull together an anchor and a "positive" sample in embedding space and push apart the anchor from many "negative" samples. Nevertheless, it is infeasible for pathology images since they usually consist of multiple positive instances Li et al. (2022). SupCon extends the self-supervised batch contrastive approach to the fully-supervised setting, allowing us to effectively leverage label information Khosla et al. (2020). But fine-grained local annotations for WSIs are hardly available. We exploit the low-rank properties to generalize the supervised contrastive loss for WSIs without no patch-level label information.

2.2 Global Feature Aggregation in MIL

Traditional pooling (e.g. mean, max pooling) is non-parametric, and not robust to noisy data and unbalanced distribution. MIL-RNN Campanella et al. (2019) built on recurrent network achieved clinical-grade using with more than 10,000 slides, but it is data-hungry and constrained for binary classification. The local attention method i.e. ABMIL Ilse et al. (2018) uses the attention weights to allow us to find key instances, bringing great improvements and robustness. CLAM Lu et al. (2021c) further improves ABMIL with a clustering constrain by pulling the most and least attended instances apart. As concluded by Lu et al. (2021c), one limitation of CLAM and MIL-based approaches is that they typically treat different patches in the slide as independent and do not learn potential nonlinear interactions between instances, which may help the model become more context-aware. To this end, global attention-based networks, e.g. DSMIL Li et al. (2021), transMIL Shao et al. (2021), SMILE Lu et al. (2021a), are introduced with non-local pooling or transformer encoder to compensate for the shortness of attention-based MIL that considers no correlation between instances.

3 Method

The proposed pipeline is boosted with the low-rank property of WSI, consisting of a local feature embedding module and a global feature aggregation module as illustrated in Fig. 1.

3.1 LOCAL FEATURE EMBEDDING

3.1.1 PRELIMINARY

Contrastive learning implements the heuristic to discern positive samples from negative samples Chen et al. (2020a;b;c;c); Grill et al. (2020); Gao et al. (2021). Given a randomly sampled minibatch of N images, we get pairs of projected feature vectors from augmented examples $\{\boldsymbol{z}_i\}_{i\in I}, I = \{1, \cdots, 2N\}$. The self-supervised contrastive loss is Chen et al. (2020a):

$$\mathcal{L}_{\text{Con}} = -\sum_{i\in I} \log \frac{\exp\left(\text{sim}(\boldsymbol{z}_i, \boldsymbol{z}_{j(i)})/\tau\right)}{\sum_{a\in\mathcal{N}(i)} \exp\left(\text{sim}(\boldsymbol{z}_i, \boldsymbol{z}_a)/\tau\right)} \tag{1}$$

where $\text{sim}(\boldsymbol{u}, \boldsymbol{v}) = \boldsymbol{u}^\top \boldsymbol{v}/\|\boldsymbol{u}\|\|\boldsymbol{v}\|$ is the dot product between ℓ_2 normalized $\boldsymbol{u}$ and $\boldsymbol{v}$; $\mathcal{N}(i) = I\backslash\{i\}$; $j(i)$ is the index of the other augmented sample from the same image; τ is a temperature parameter. For each anchor $\boldsymbol{z}_i$, there is one positive sample $\boldsymbol{z}_{j(i)}$ and $2(N-1)$ negative samples.

3.1.2 EXTENSION OF CONTRASTIVE LOSS

Most cases in pathology have high semantic and background similarity thus resulting in multiple positives in a batch, introducing estimation errors in (1). One straightforward approach is the generalization of supervised contrastive learning (i.e., SupCon Khosla et al. (2020)) to an arbitrary number of positives by extending:

$$\mathcal{L}_{\text{SupCon}} = -\sum_{i\in I} \frac{1}{|\mathcal{P}(i)|} \sum_{p\in\mathcal{P}(i)} \log \frac{\exp\left(\text{sim}(\boldsymbol{z}_i, \boldsymbol{z}_p)/\tau\right)}{\sum_{a\in\mathcal{N}(i)} \exp\left(\text{sim}(\boldsymbol{z}_i, \boldsymbol{z}_a)/\tau\right)} \tag{2}$$

where $\mathcal{P}(i)$ is the set of indices of all positive samples in the minibatch given anchor $\boldsymbol{z}_i$; $|\mathcal{P}(i)|$ is its cardinality. For images with labels, it is intuitive to constitute positive samples with the same labels.

3.1.3 PATHOLOGY SPECIFIC LOW-RANK LOSS

SupCon in (2) extents vanilla contrastive loss by leveraging label information. *But we refrain from adopting SupCon for WSIs because no patch-level labels are available.* We thus propose a new self-supervised learning loss named LRC tailored for pathology images, which is shown to be a generalization of SupCon to unlabeled scenarios.

Given a set of feature samples, each of which can be represented as a linear combination of the bases in a dictionary, we aim at finding the representations that have low-rank similarity matrix between two sets of augmented representations:

$$\mathcal{R}(\mathbf{T}^\top\tilde{\mathbf{T}}) = \left\{\mathbf{T}^\top\tilde{\mathbf{T}} \in \mathbb{R}^{N\times N} : \text{rank}(\mathbf{T}^\top\tilde{\mathbf{T}}) = r, r \ll N\right\} \tag{3}$$

where $\mathbf{T}^\top\tilde{\mathbf{T}}$ is a similarity matrix of $\mathbf{T} = [\boldsymbol{t}_1, \cdots, \boldsymbol{t}_N]$, $\tilde{\mathbf{T}} = [\tilde{\boldsymbol{t}}_1, \cdots, \tilde{\boldsymbol{t}}_N]$; $\tilde{\boldsymbol{t}}_i$ and $\boldsymbol{t}_i$ are two augmented representations of the same image. A low-rank matrix can be decomposed as the product of a dictionary $\mathbf{D}$ and a block-diagonal $\mathbf{B}$ such that Liu et al. (2012); Wright & Ma (2022):

$$\mathbf{T}^\top\tilde{\mathbf{T}} = \mathbf{D}\mathbf{B} + \mathbf{E} = [\mathbf{D}_1, \mathbf{D}_2, \cdots, \mathbf{D}_r] \begin{bmatrix} \mathbf{B}_1 & \mathbf{0} & \mathbf{0} & \mathbf{0} \\ \mathbf{0} & \mathbf{B}_2 & \mathbf{0} & \mathbf{0} \\ \mathbf{0} & \mathbf{0} & \ddots & \mathbf{0} \\ \mathbf{0} & \mathbf{0} & \mathbf{0} & \mathbf{B}_r \end{bmatrix} + \mathbf{E} \tag{4}$$

where $\mathbf{E}$ is an error matrix which should be minimized; $\mathbf{D}_b \in \mathbb{R}^{N\times s_b}$, $\mathbf{B}_b \in \mathbb{R}^{s_b\times q_b}$ with $b = 1, \cdots, r$; s_b, q_b represent the shape of subspace $\mathbf{B}_b$.

Intuitively, pairs belonging to the same subspace are more semantically similar than randomly sampled ones. This has also been recognized as latent classes Chuang et al. (2020); Saunshi et al. (2019). For self-supervised contrastive loss $\mathcal{L}_{\text{Con}}$ with only one positive pair for each anchor, $\mathbf{T}^\top\tilde{\mathbf{T}}$ is considered to be a full-rank diagonal matrix, i.e., all entries are zeros except for the diagonal ones. SupCon loss $\mathcal{L}_{\text{SupCon}}$ further leverages label information to access more positive samples, enforcing $\mathbf{T}^\top\tilde{\mathbf{T}}$ to explore the semantic similarity in the embedding space. In this way, SupCon loss could

make low-rank constraints implicitly on $\mathbf{T}^\top \tilde{\mathbf{T}}$, where r is the rank of the matrix corresponding to the total number of classes in SupCon. This observation recognizes the connections of contrastive loss with the low-rank property.

Since the low-rank decomposition of (3) is not tractable for online learning, as an alternative, we use SupCon loss in (2) as a surrogate by accessing more positives belonging to the same subspace $\mathbf{B}_b$. Suppose we get a set of descendingly *sorted* indices based on their similarity to the anchor:

$$C(a) = \{a_1, \cdots, a_N\}; \forall_{i,j \in \{1,\cdots,N\}}, \text{if } i < j, \text{sim}(\boldsymbol{t}_a, \tilde{\boldsymbol{t}}_{a_i}) \geq \text{sim}(\boldsymbol{t}_a, \tilde{\boldsymbol{t}}_{a_j}). \tag{5}$$

Without loss of generality, we split it into r subspace to align with the rank of $\mathbf{T}^\top \tilde{\mathbf{T}}$ where $C_1(a) = \{a_1, \cdots, a_{q_1}\}$, $C_2(a) = \{a_{q_1}+1, \cdots, a_{q_1}+a_{q_2}\}$, $\cdots$, $C_r(a) = \{N - a_{q_r}+1, \cdots, N\}$. Note that $q_1, q_2, \cdots q_r$, is the column dimension of $\mathbf{B}_1, \mathbf{B}_2, \cdots, \mathbf{B}_r$. Instead of partitioning all samples to get all subspace, which is computationally infeasible without solving (4), we only optimize the objective over the most- and least-distant subspace $C_1(a), C_r(a)$ with respect to the anchor. For any positive sample $p \in C_1(a)$ and negative sample $n \in C_r(a)$, we would like to achieve the following:

$$\text{sim}(\boldsymbol{t}_a, \tilde{\boldsymbol{t}}_p) \geq \text{sim}(\boldsymbol{t}_a, \tilde{\boldsymbol{t}}_n) + \xi, \tag{6}$$

where $\xi = 0.5$ is a constant margin for all pairs of negative. Based on the fact that $\text{sim}(\boldsymbol{t}_a, \tilde{\boldsymbol{t}}_i) \geq \text{sim}(\boldsymbol{t}_a, \tilde{\boldsymbol{t}}_j) \geq \text{sim}(\boldsymbol{t}_a, \tilde{\boldsymbol{t}}_k)$, where j belongs to some subspace between C_1 and C_r, we should add some threshold ξ rather than just ensure $\text{sim}(\boldsymbol{t}_a, \tilde{\boldsymbol{t}}_p) \geq \text{sim}(\boldsymbol{t}_a, \tilde{\boldsymbol{t}}_n)$ to avoid trivial solution for the loss.

We can incorporate low-rank constraint loss with margin into the supervised contrastive loss function in (2) by adding it after the cosine similarity term, giving us:

$$\mathcal{L}_{\text{LRC}} = -\sum_{a=1\cdots N} \frac{1}{|C_1(a)|} \sum_{p \in C_1(a)} \log \frac{\exp\left(\text{sim}(\boldsymbol{t}_a, \tilde{\boldsymbol{t}}_p)\right)}{\sum_{j \in \{C_1(a) \cup C_r(a)\} \setminus a} \exp\left(\text{sim}(\boldsymbol{t}_a, \tilde{\boldsymbol{t}}_j) + \xi_j\right)}. \tag{7}$$

where $\xi_j = 0$ if $j \in C_1(a)$, otherwise $\xi_j = \xi$. The loss (7) is minimized when all positive pairs are correctly identified with condition (6) satisfied, thus enforcing our low-rank constraints. We set the top 5% of instances in a training batch as C_1 and the bottom 5% as C_r. The derivation and analysis of (7) is provided in the Appendix A, C.

The total loss for self-supervised learning for feature embedding is:

$$\mathcal{L} = \lambda \mathcal{L}_{\text{con}} + (1-\lambda)\mathcal{L}_{\text{LRC}}. \tag{8}$$

Without the self-supervised contrastive loss (1), there is a chicken-and-egg issue that good features will not be learned and low-rank loss in (28) is not sufficiently good. Incorporating contrastive loss $\mathcal{L}_{\text{con}}$ with $\mathcal{L}_{\text{LRC}}$ is an incremental self-updating learning process. In our default setting where $\lambda = 0.5$, no unstable training is observed.

3.2 Global Feature Aggregation

3.2.1 Preliminary

Without loss of generality, we take the binary MIL classification as an example. The learning task is to learn a nonlinear function from feature space $\mathcal{X}$ to label space $\mathcal{Y} = \{1, 0\}$ using the training data set $\{(X_1, y_1), \cdots, (X_m, y_m)\}$, where $X_i = \{\boldsymbol{x}_{i,1}, \cdots, \boldsymbol{x}_{i,m_i}\}$ is a WSI; m_i is the bag size of X_i; $\boldsymbol{x}_{i,j}$ is an instance. The corresponding instance labels $\{y_{i,1}, \cdots y_{i,m_i}\}$ are *unknown*, i.e.

$$y_i = \begin{cases} 0, \text{ iff } \sum_j y_{i,j} = 0; y_{i,j} \in \{0,1\}, j = 1, \cdots m_i \\ 1, \text{ otherwise .} \end{cases} \tag{9}$$

MIL processes a bag of instances with permutation invariance property, stating that the label of the bag is the remain unchanged regardless of the order of input instances on the bag Ilse et al. (2018); Li et al. (2021). A simple example of a permutation invariant model is a network that performs pooling over embedding extracted from the patches of a bag. Mathematically:

$$\text{logits}(X_i) = \rho\left(\text{pool}\left(\{\phi\left(\boldsymbol{x}_{i,1}\right), \cdots, \phi\left(\boldsymbol{x}_{i,m_i}\right)\}\right)\right), \tag{10}$$

where 'pool' is pooling operation; ϕ and ρ denote instance-level network and bag-level classifier, respectively. Attention-based pooling is commonly used Ilse et al. (2018); Lu et al. (2021c); Tomita et al. (2019); Hashimoto et al. (2020):

$$\phi(x_{i,j}) = \frac{\exp\left\{\mathbf{W}^\top \left(\tanh\left(\mathbf{V}\boldsymbol{x}_{i,j}\right) \odot \operatorname{sigm}\left(\mathbf{U}\boldsymbol{x}_{i,j}\right)\right)\right\}}{\sum_{j=1}^{m_i} \exp\left\{\mathbf{W}^\top \left(\tanh\left(\mathbf{V}\boldsymbol{x}_{i,j}\right) \odot \operatorname{sigm}\left(\mathbf{U}\boldsymbol{x}_{i,j}\right)\right)\right\}}, \tag{11}$$

with learnable parameters $\mathbf{W}$, $\mathbf{V}$, and $\mathbf{U}$.

3.2.2 TRANSFORMER-BASED MIL

Eq. (11) is a local attention network where the score $\phi(\boldsymbol{x}_{i,j})$ of instance $\boldsymbol{x}_{i,j}$ only depends on the instance itself. We aim to explore the dependence and correlation among all instances. One straightforward approach is the application of transformer.

The transformer encoder consists of alternating layers of multi-headed attention and MLP blocks. Here, we denote the feature matrix of the feature bag X_i as $\mathbf{X}_i^1 = [\boldsymbol{x}_{i,1}, \cdots, \boldsymbol{x}_{i,m_i}]^\top$. An attention head maps queries $\mathbf{Q} \in \mathbb{R}^{m_i \times d}$ to outputs using m_i key-value pairs $\mathbf{K} \in \mathbb{R}^{m_i \times d}$, $\mathbf{V} \in \mathbb{R}^{m_i \times d}$, and d is the query/key dimension:

$$\begin{cases} \operatorname{head}_h(\mathbf{X}_i^\ell) = \text{Attention}(\mathbf{Q}_h, \mathbf{K}_h, \mathbf{V}_h) = \text{softmax}\left(\mathbf{Q}_h \mathbf{K}_h^\top / \sqrt{d}\right) \mathbf{V}_h \\ \text{where } \mathbf{Q}_h = \mathbf{X}_i^\ell \mathbf{W}_{h,\ell}^Q,\ \mathbf{K}_h = \mathbf{X}_i^\ell \mathbf{W}_{h,\ell}^K,\ \mathbf{V}_h = \mathbf{X}_i^\ell \mathbf{W}_{h,\ell}^V,\ h = 1, \cdots, H, \end{cases} \tag{12}$$

where $\mathbf{W}_{h,\ell}^Q$, $\mathbf{W}_{h,\ell}^K$, $\mathbf{W}_{h,\ell}^V$ are learnable; $\ell = 1, \cdots, k$ is the index of the transformer layer; k is the total number of layers. Transformer uses multi-head attention to project $\mathbf{Q}; \mathbf{K}; \mathbf{V}$ onto H different vectors and then concatenate all attention outputs:

$$\begin{cases} \operatorname{MHA}(\mathbf{X}_i^\ell) = \operatorname{concat}\left(\operatorname{head}_1, \cdots, \operatorname{head}_H\right) \\ \hat{\mathbf{X}}_i^\ell = \operatorname{MHA}\left(\operatorname{LN}\left(\mathbf{X}_i^\ell\right)\right) + \mathbf{X}_i^\ell, \end{cases} \tag{13}$$

where LN is the layer norm. The output layer is MLP with skip connection:

$$\mathbf{X}_i^{\ell+1} = \operatorname{MLP}\left(\operatorname{LN}\left(\hat{\mathbf{X}}_i^\ell\right)\right) + \hat{\mathbf{X}}_i^\ell. \tag{14}$$

Considering a large number of instances in each bag (hundreds of thousands), one obstacle with transformer for MIL is the quadratic time and memory complexity $O\left(m_i^2\right)$. Despite the linear theoretical complexity with some approximations like Nystromformer Xiong et al. (2021), Linformer Wang et al. (2020a), or Performer Choromanski et al. (2020), it overlooks the innate characteristic of input instances.

3.2.3 ITERATIVE LOW-RANK ATTENTION MIL

Medical images including WSI have long been known as low-rank that can be projected onto a subspace much lower than its original space Wang et al. (2020b); Li et al. (2018; 2020). We thus introduce a learnable low-rank latent matrix $\mathbf{L} \in \mathbb{R}^{r \times d}$ to interact with all input instances as the proposed ILRA-MIL shown in Fig. 2. One basic module of the network is the cross-attention (`CAtt`), defined as:

$$\begin{cases} \operatorname{CAtt}(\mathbf{L}, \mathbf{X}_i^\ell) = \text{Attention}(\mathbf{Q}, \mathbf{K}, \mathbf{V}) = \text{softmax}\left(\mathbf{Q}\mathbf{K}^\top / \sqrt{d}\right) \mathbf{V} \\ \text{where } \mathbf{Q} = \mathbf{L}\mathbf{W}_\ell^Q,\ \mathbf{K} = \mathbf{X}_i^\ell \mathbf{W}_\ell^K,\ \mathbf{V} = \mathbf{X}_i^\ell \mathbf{W}_\ell^V. \end{cases} \tag{15}$$

Note that $\mathbf{L}$ is a unified matrix for all layers to keep the low-rank consistency for different layers. As shown in right-hand side of Fig. 2, we also use a unified layer with cross-attention and Gated Linear United (GLU), named Gated Attention Block (GAB):

$$\begin{cases} \operatorname{GAB}(\mathbf{L}, \mathbf{X}_i^\ell) = (\mathbf{U} \bigodot \hat{\mathbf{V}})\mathbf{W}_\ell^O \\ \mathbf{U} = \phi_U(\mathbf{L}\mathbf{W}_\ell^U), \hat{\mathbf{V}} = \operatorname{CAtt}(\mathbf{L}, \mathbf{X}_i^\ell) \end{cases} \tag{16}$$

where $\bigodot$ stands for element-wise multiplication ; ϕ_U is Sigmoid Linear Units `SiLU` Elfwing et al. (2018); Hua et al. (2022); $\mathbf{W}_\ell^O, \mathbf{W}_\ell^U$ are linear transforms. The inputs of GAB are *not* permutation invariant as the first is the query and the second is the key-value. An `ILRA` block consists of:

$$\mathbf{P} = \operatorname{GAB}_{\text{f}}(\mathbf{L}, \mathbf{X}_i^\ell),\ \mathbf{X}_i^{\ell+1} = \operatorname{GAB}_{\text{b}}(\mathbf{X}_i^\ell, \mathbf{P}). \tag{17}$$

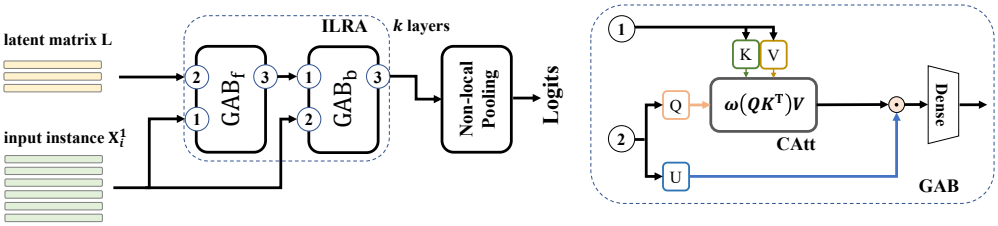

Figure 2: ILRA-MIL iterates over k IRLA layers. Each layer consists of two GAB blocks. The first GAB block projects input instance $\mathbf{X}_i^1 \in \mathbb{R}^{m_i \times d}$ to low-rank space by attending to the latent vectors $\mathbf{L} \in \mathbb{R}^{r \times d}$, $r < m_i$ and the second GAB recovers the input dimension. ω represents `softmax`. The output layer uses non-local pooling to make predictions. Layer normalization is omitted for brevity.

Eq. (17) is analogous to low-rank projection or auto-encoder models. GAB_f first projects the high-dimensional $\mathbf{X}_i^\ell$ to the low-rank space $\mathbf{L}$. Then the projection result $\mathbf{P} \in \mathbb{R}^{r \times d}$ is reconstructed to high-dimensional space $\mathbf{X}_i^{\ell+1}$ with GAB_b where the query is $\mathbf{X}_i^\ell$ and key-value is $\mathbf{P}$.

There are some desirable properties of ILRA-MIL. (i) The latent vectors $\mathbf{L}$ encode global features that help to explain input instances. For example, in the cancer subtyping problem for computational pathology, the latent vectors could be approximately some mutual and universal information of key cancerous regions so that the `ILRA` module can compare instances in the query indirectly through $\mathbf{L}$ to all inputs. (ii) The $\mathbf{Q}$-$\mathbf{K}$-$\mathbf{V}$ pair is not longer symmetric as in `MHA` because for the shapes $\mathbf{L} \in \mathbb{R}^{r \times d}$, $\mathbf{K} \in \mathbb{R}^{m_i \times d}$, $\mathbf{V} \in \mathbb{R}^{m_i \times d}$, $r \ll m_i$. Thus, the complexity of cross-attention operation significantly is reduced from quadratic $\mathcal{O}(m_i^2)$ to linear $\mathcal{O}(rm_i)$. We set $r = 64$ by default.

Constraining the latent vectors to be low-rank may restrict the network's ability to capture all of the necessary details from the input instances. To improve expressivity, the model stacks k `ILRA` layers to extract information from the input instances with light computation overhead:

$$\mathbf{X}_i^k = \underbrace{\text{ILRA}(\text{ILRA}(\mathbf{X}_i^1)\cdots)}_{\text{k layers}}, \tag{18}$$

where LN should be applied before the input of each layer. $\mathbf{X}_i^k = \{\tilde{\boldsymbol{x}}_1, \tilde{\boldsymbol{x}}_2, \cdots, \tilde{\boldsymbol{x}}_{m_i}\}$ encodes higher-order interactions instances in the bag. A trainable bag feature $\boldsymbol{x}_\text{b}$ is defined to conduct non-local pooling at the output layer:

$$\text{logits}(\mathbf{X}_i) = \rho(\sum_{j=1}^{m_i} w_j \cdot \tilde{\boldsymbol{x}}_j), \quad w_j = \frac{\exp(\boldsymbol{x}_\text{b} \cdot \tilde{\boldsymbol{x}}_j)}{\sum_{q=0}^{m_i} \exp(\boldsymbol{x}_\text{b} \cdot \tilde{\boldsymbol{x}}_q)}. \tag{19}$$

4 Experiments

4.1 Dataset

CAMELYON16 is a public dataset for metastasis detection in breast cancer (binary classification), including 270 training slides and 130 test slides. A total of about 1.5 million patches at $\times 10$ magnification are obtained. **TCGA-NSCLC** includes two subtype projects (binary classification), i.e., Lung Squamous Cell Carcinoma (TGCA-LUSC) and Lung Adenocarcinoma (TCGA-LUAD), for a total of 993 diagnostic WSIs, including 507 LUAD slides from 444 cases and 486 LUSC slides from 452 cases. We obtain 3.4 million patches in total at $\times 10$ magnification. **PANDA** is the largest prostate biopsy public dataset to date Bulten et al. (2022). We use 4369 slides from Karolinska Institute for training. The independent test set from Radboud University has 2591 slides. A total of 1.1 million patches at $\times 10$ magnification are obtained. *More details are introduced in the Appendix.*

4.2 Implementation Details

Training. In CAMELYON16, the 270 training WSIs are split into approximately 90% training and 10% validation, and tested on the official test set. In PANDA, we split the 4219 slides from Karolinska into 80% training and 20% validation, and tested on the 2591 slides from Radboud. For

Table 1: Classification Results on Benchmarks.

	CAMELYON16		TCGA-NSCLC		PANDA	
	Acc	AUC	Acc	AUC	Acc	kappa
Mean-pooling	0.6511	0.6755	0.7282	0.8401	0.5691	0.4422
Max-pooling	0.7674	0.8169	0.8593	0.9263	0.6100	0.5830
ABMIL	0.8527	0.8503	0.8384	0.9205	0.6834	0.5998
MIL-RNN	0.8449	0.8580	0.8619	0.9107	NA	NA
CLAM-SB	0.8682	0.8709	0.8632	0.9307	0.6648	0.5782
CLAM-MB	0.8604	0.8779	0.8492	0.9377	0.6760	<u>0.6067</u>
DSMIL	0.8759	0.8944	0.8690	0.9439	0.6737	0.5562
DSMIL+SimCLR	0.8867	0.9175	<u>0.9048</u>	0.9551	<u>0.7017</u>	0.5837
TransMIL	0.8449	0.8769	0.8565	0.9303	0.6720	0.5638
DTFD-MIL	<u>0.9010</u>	<u>0.9401</u>	0.8941	<u>0.9612</u>	0.6573	0.5437
ILRA-MIL	**0.8992**	**0.9278**	**0.9004**	**0.9592**	**0.7094**	**0.6236**
ILRA-MIL + LRC	**0.9218**	**0.9649**	**0.9213**	**0.9763**	**0.7287**	**0.6562**

TCGA datasets, we first ensured that different slides from one patient do not exist in both the training and test sets, and split the data in the ratio of training:validation:test = 60:15:25. For self-supervised learning, we use ResNet50 to encode 224×224 patch into 1024-dimensional vector. The same training data is used to develop feature embedding with LRC and feature aggregator ILRA-MIL.

Evaluation. For the evaluation metrics, we used accuracy and area under the curve (AUC) scores to evaluate the classification performance, where the accuracy was calculated with a threshold of 0.5 in all experiments. The multi-class PANDA are scored based on the Cohen's kappa.

Baseline methods include mean/max-pooling and deep MIL models, i.e., ABMIL Ilse et al. (2018), DSMIL Li et al. (2021), CLAM-SB / CLAM-MB Lu et al. (2021c), MIL-RNN Campanella et al. (2019), transMIL Shao et al. (2021), and DTFD-MIL Zhang et al. (2022).

5 Results

5.1 Results on Classification

All results are provided in Table 5. "DSMIL+SimCLR" denotes DSMIL with SimCLR features as reported in Li et al. (2021). Other baselines use ImageNet pre-trained features if without notice. In all cases, ILRA with LRC feature embedding consistently improves over ImageNet pre-trained feature embedding, as the statistic in the last row shows.

In CAMELYON16, tumors are minor regions in positive slides (averagely $< 10\%$ per slide), resulting in a highly imbalanced distribution of positive and negative instances in a bag. Attention-based methods all outperform the traditional mean or max pooling operators. Non-local poolings including DSMIL and transMIL outperform attention pooling with nonlocal operator that models the interaction between instances. DTFD-MIL is the best-performed competing method which is particularly designed to address the small sample cohorts. The proposed ILRA-MIL processes higher interactions and in AUC score, it was at least 4.99% higher than CLAM-MB which neglects the cross-instance correlations.

In TCGA-NSCLC, positive slides contain relatively large areas of tumor region (averagely total cancer area per slide $> 80\%$). As a result, both the max pooling and attention pooling operators work quite well in this scenario. Non-local pooling methods are consistently stable, and ILRA-MIL performed better than all the other competing methods, achieving 1.53% improvement in AUC and 1.51% in accuracy, compared with the best competing results .

For PANDA, as MIL-RNN does not work for multi-classification problems, we exclude it from the comparison result. PANDA is unbalanced distributed in cancer subtypes, and it is difficult to differentiate glandular patterns with intermediate morphological structures Nagpal et al. (2020).

ILRA-MIL can also be applied to multi-class problems with unbalanced data and it can be observed that the best results are achieved in both accuracy and kappa. For comparison, existing clinical-

Table 2: Ablation on Different Pretrained Models.

	ILRA-MIL		CLAM-SB	
	Acc	AUC	Acc	AUC
ImageNet	0.8992	0.9278	0.8682	0.8709
SimCLR Chen et al. (2020a)	0.9082	0.9392	0.8895	0.9106
BYOL Grill et al. (2020)	0.9002	0.9330	0.8701	0.8902
SimSiam Chen & He (2021)	0.9032	0.9354	0.8837	0.8962
MoCov3 Chen et al. (2020c)	0.9158	0.9490	0.9021	0.9123
LRC (ours)	**0.9218**	**0.9649**	**0.9088**	**0.9377**

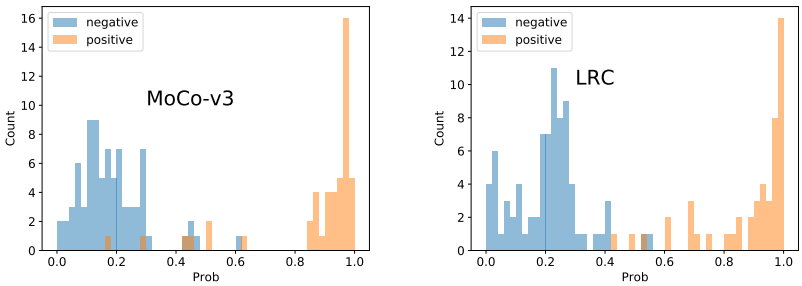

Figure 3: Probability distribution with MoCo-v3 and LRC.

grade AI system trained pixel-wise annotations from highly urological pathologists scores from 0.62 Bulten et al. (2020) to 0.66 Tolkach et al. (2020).

5.2 Ablations on LRC

To demonstrate the effectiveness of the proposed clustering-constrained contrastive loss, we compare its performance with alternative contrastive learning: SimCLR Chen et al. (2020a), BYOL Grill et al. (2020), SimSiam Chen & He (2021), and MoCoV3 Chen et al. (2020c), and a ImageNet pre-trained model, as shown in Table 2. The same ILRA-MIL model is used to evaluate the ACC and AUC performance. Unsurprisingly, all self-supervised features bootstrap the performance against the ImageNet pre-trained features remarkably.

BYOL and SimSiam without negative samples are outperformed by MoCo-V3 and SimCLR. The proposed LRC achieves 1.59% AUC improvement over MoCo-v3. Similar results also apply to CLAM-SB as shown in the table. Fig. 3 shows the predicted probability on the CAMELYON16 test set using ILRA-MIL trained with MoCo-v3 features and LRC features. As we set 0.5 as the classification threshold, we can observe that with LRC features, there are fewer false positives and false negatives samples compared with the probability distribution of MoCo-V3.

5.3 Parameter Analysis and Ablations on ILRA-MIL

We conduct some ablations on ILRA-MIL in terms of some key modules: (i) low-rank latent vectors attention in (15); (ii) non-local pooling in (19); (iii) iterative attention mechanism in (18). Ablation studies are performed on the CAMELYON16 dataset with ImageNet features, see Table 3.

(1) The default rank of $\mathbf{L}$ in Eq. (15) is $r = 64$. We adjust the rank from 32 to 128 and the result demonstrates that with a large-enough vector rank, it is capable of attending all input instances with negligible loss of information. Then, we compare it with the self-attention module.

(2) We cannot directly apply the full self-attention considering the large bag size and instead, we use Nystrom transformer as an approximation. The same number of heads and layers are used for evaluation. The results indicated that low-rank attention achieves 0.9278 AUC, outperforming 0.8127 AUC of full self-attention by a large margin. Although with linear approximation, full self-attention involves excessively redundant and task-irrelevant interactions among instances and is difficult to optimize where only a small amount of slide-level labels available.

Table 3: Parameter Analysis and Ablations on ILRA-MIL

	Settings	# params	AUC
(i)	rank $r = 16$	2.97 M	0.9205
	rank $r = 32$	2.99 M	0.9231
	rank $r = 64$	3.02 M	0.9278
	rank $r = 128$	3.09 M	0.9279
(ii)	full self-attention	2.64 M	0.8127
	low-rank attention	3.02 M	**0.9278**
(iii)	max pooling	2.76 M	0.8061
	local att. Pooling	5.01 M	0.8612
	nonlocal att. pooling	3.02 M	**0.9278**

	Settings	# params	AUC
(iv)	iteration $k = 1$	1.39 M	0.9102
	iteration $k = 2$	1.94 M	0.9221
	iteration $k = 4$	3.02 M	**0.9278**
	iteration $k = 6$	4.11 M	0.8947
	iteration $k = 8$	5.19 M	0.8418

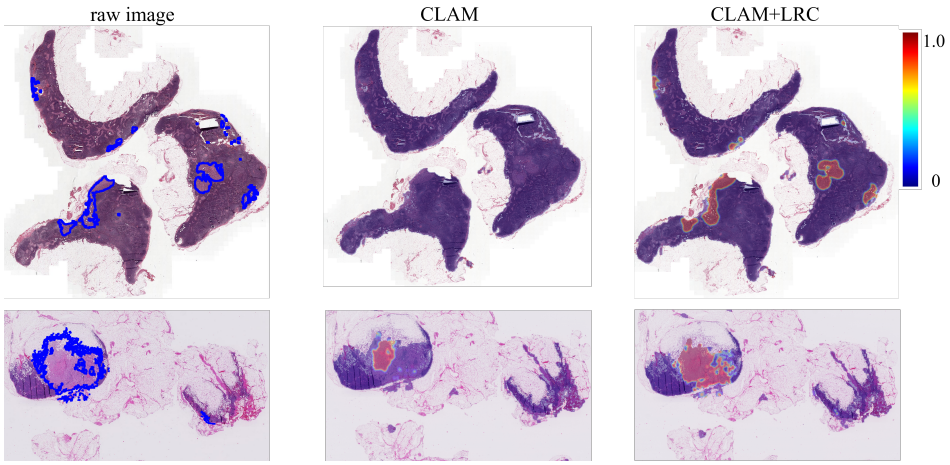

Figure 4: Heatmap visualization of "test_075" and "test_026" for CLAM with and without LRC.

(3) After `ILRA` iteration in (17), non-local pooling is used with (19) to aggregate global feature. We ablate it with the commonly used max pooling and local attention pooling in (11). Remarkably, nonlocal pooling can improve max pooling and local attention pooling by 12.17% and 6.66% AUC.

(4) ILRA-MIL can make a deeper network through iterative attention. As the number of iterations increases, the model performance growth tends to level off, which indicates that the it is sufficient to characterize patch interactions in the dataset. The iteration number greater than $k = 4$ leads to a significant decrease in performance, which is caused by the over-fitting on the dataset.

5.4 Interpretability

Our feature embedding LRC boosts the performance of CLAM-SB (see Table 2) and it can also enhance interpretability. We use the trained CLAM-SB model with LRC features to draw the predicted heatmap as shown in Fig. 4. The heatmaps show remarkable consistency with expert annotation, especially for "test_075" where the ROIs only occupied a small area, the most significant regions are located and identified. We show more visual comparisons in the Appendix.

6 Conclusion

In this paper, we address the problem of WSI classification by optimizing the feature embedding and feature aggregation with low-rank property. We improve the vanilla contrastive loss with additional low-rank constraints to collect more positive samples for contrast, and we further devise an iterative low-rank attention feature aggregator to make efficient non-local interactions among instances. All these designs boost the performance across various benchmarks as the results show. One limitation of our model is that it has not been validated on *multi-center* larger-scale clinical datasets. In addition, ILRA-MIL cannot directly provide a local attention score for each instance, which might hinder an intuitive clinical analysis of each individual patch image.

REFERENCES

Stephen Boyd, Neal Parikh, Eric Chu, Borja Peleato, Jonathan Eckstein, et al. Distributed optimization and statistical learning via the alternating direction method of multipliers. *Foundations and Trends® in Machine learning*, 3(1):1–122, 2011.

Wouter Bulten, Hans Pinckaers, Hester van Boven, Robert Vink, Thomas de Bel, Bram van Ginneken, Jeroen van der Laak, Christina Hulsbergen-van de Kaa, and Geert Litjens. Automated deep-learning system for gleason grading of prostate cancer using biopsies: a diagnostic study. *The Lancet Oncology*, 21(2):233–241, 2020.

Wouter Bulten, Kimmo Kartasalo, Po-Hsuan Cameron Chen, Peter Ström, Hans Pinckaers, Kunal Nagpal, Yuannan Cai, David F Steiner, Hester van Boven, Robert Vink, et al. Artificial intelligence for diagnosis and gleason grading of prostate cancer: the panda challenge. *Nature medicine*, pp. 1–10, 2022.

Gabriele Campanella, Matthew G Hanna, Luke Geneslaw, Allen Miraflor, Vitor Werneck Krauss Silva, Klaus J Busam, Edi Brogi, Victor E Reuter, David S Klimstra, and Thomas J Fuchs. Clinical-grade computational pathology using weakly supervised deep learning on whole slide images. *Nature medicine*, 25(8):1301–1309, 2019.

Emmanuel J Candès, Xiaodong Li, Yi Ma, and John Wright. Robust principal component analysis? *Journal of the ACM (JACM)*, 58(3):1–37, 2011.

Ting Chen, Simon Kornblith, Mohammad Norouzi, and Geoffrey Hinton. A simple framework for contrastive learning of visual representations. In *International conference on machine learning*, pp. 1597–1607. PMLR, 2020a.

Ting Chen, Simon Kornblith, Kevin Swersky, Mohammad Norouzi, and Geoffrey E Hinton. Big self-supervised models are strong semi-supervised learners. *Advances in neural information processing systems*, 33:22243–22255, 2020b.

Xinlei Chen and Kaiming He. Exploring simple siamese representation learning. In *Proceedings of the IEEE/CVF Conference on Computer Vision and Pattern Recognition*, pp. 15750–15758, 2021.

Xinlei Chen, Haoqi Fan, Ross Girshick, and Kaiming He. Improved baselines with momentum contrastive learning. *arXiv preprint arXiv:2003.04297*, 2020c.

Krzysztof Choromanski, Valerii Likhosherstov, David Dohan, Xingyou Song, Andreea Gane, Tamas Sarlos, Peter Hawkins, Jared Davis, Afroz Mohiuddin, Lukasz Kaiser, et al. Rethinking attention with performers. *arXiv preprint arXiv:2009.14794*, 2020.

Ching-Yao Chuang, Joshua Robinson, Yen-Chen Lin, Antonio Torralba, and Stefanie Jegelka. Debiased contrastive learning. *Advances in neural information processing systems*, 33:8765–8775, 2020.

Ozan Ciga, Tony Xu, and Anne Louise Martel. Self supervised contrastive learning for digital histopathology. *Machine Learning with Applications*, 7:100198, 2022.

Yang Cong, Ji Liu, Junsong Yuan, and Jiebo Luo. Self-supervised online metric learning with low rank constraint for scene categorization. *IEEE Transactions on Image Processing*, 22(8):3179–3191, 2013.

Stefan Elfwing, Eiji Uchibe, and Kenji Doya. Sigmoid-weighted linear units for neural network function approximation in reinforcement learning. *Neural Networks*, 107:3–11, 2018.

Tianyu Gao, Xingcheng Yao, and Danqi Chen. Simcse: Simple contrastive learning of sentence embeddings. *arXiv preprint arXiv:2104.08821*, 2021.

Jean-Bastien Grill, Florian Strub, Florent Altché, Corentin Tallec, Pierre Richemond, Elena Buchatskaya, Carl Doersch, Bernardo Avila Pires, Zhaohan Guo, Mohammad Gheshlaghi Azar, et al. Bootstrap your own latent-a new approach to self-supervised learning. *Advances in Neural Information Processing Systems*, 33:21271–21284, 2020.

Noriaki Hashimoto, Daisuke Fukushima, Ryoichi Koga, Yusuke Takagi, Kaho Ko, Kei Kohno, Masato Nakaguro, Shigeo Nakamura, Hidekata Hontani, and Ichiro Takeuchi. Multi-scale domain-adversarial multiple-instance cnn for cancer subtype classification with unannotated histopathological images. In *Proceedings of the IEEE/CVF conference on computer vision and pattern recognition*, pp. 3852–3861, 2020.

Weizhe Hua, Zihang Dai, Hanxiao Liu, and Quoc V Le. Transformer quality in linear time. *arXiv preprint arXiv:2202.10447*, 2022.

Maximilian Ilse, Jakub Tomczak, and Max Welling. Attention-based deep multiple instance learning. In *International conference on machine learning*, pp. 2127–2136. PMLR, 2018.

Prannay Khosla, Piotr Teterwak, Chen Wang, Aaron Sarna, Yonglong Tian, Phillip Isola, Aaron Maschinot, Ce Liu, and Dilip Krishnan. Supervised contrastive learning. *Advances in Neural Information Processing Systems*, 33:18661–18673, 2020.

Bin Li, Yin Li, and Kevin W Eliceiri. Dual-stream multiple instance learning network for whole slide image classification with self-supervised contrastive learning. In *Proceedings of the IEEE/CVF Conference on Computer Vision and Pattern Recognition*, pp. 14318–14328, 2021.

Huafeng Li, Xiaoge He, Dapeng Tao, Yuanyan Tang, and Ruxin Wang. Joint medical image fusion, denoising and enhancement via discriminative low-rank sparse dictionaries learning. *Pattern Recognition*, 79:130–146, 2018.

Huafeng Li, Xiaoge He, Zhengtao Yu, and Jiebo Luo. Noise-robust image fusion with low-rank sparse decomposition guided by external patch prior. *Information Sciences*, 523:14–37, 2020.

Zhaowen Li, Yousong Zhu, Fan Yang, Wei Li, Chaoyang Zhao, Yingying Chen, Zhiyang Chen, Jiahao Xie, Liwei Wu, Rui Zhao, et al. Univip: A unified framework for self-supervised visual pre-training. *arXiv preprint arXiv:2203.06965*, 2022.

Guangcan Liu, Zhouchen Lin, Shuicheng Yan, Ju Sun, Yong Yu, and Yi Ma. Robust recovery of subspace structures by low-rank representation. *IEEE transactions on pattern analysis and machine intelligence*, 35(1):171–184, 2012.

Mengkang Lu, Yongsheng Pan, Dong Nie, Feihong Liu, Feng Shi, Yong Xia, and Dinggang Shen. Smile: Sparse-attention based multiple instance contrastive learning for glioma sub-type classification using pathological images. In *MICCAI Workshop on Computational Pathology*, pp. 159–169. PMLR, 2021a.

Ming Y Lu, Richard J Chen, Jingwen Wang, Debora Dillon, and Faisal Mahmood. Semi-supervised histology classification using deep multiple instance learning and contrastive predictive coding. *arXiv preprint arXiv:1910.10825*, 2019.

Ming Y Lu, Tiffany Y Chen, Drew FK Williamson, Melissa Zhao, Maha Shady, Jana Lipkova, and Faisal Mahmood. Ai-based pathology predicts origins for cancers of unknown primary. *Nature*, 594(7861):106–110, 2021b.

Ming Y Lu, Drew FK Williamson, Tiffany Y Chen, Richard J Chen, Matteo Barbieri, and Faisal Mahmood. Data-efficient and weakly supervised computational pathology on whole-slide images. *Nature biomedical engineering*, 5(6):555–570, 2021c.

Kunal Nagpal, Davis Foote, Fraser Tan, Yun Liu, Po-Hsuan Cameron Chen, David F Steiner, Naren Manoj, Niels Olson, Jenny L Smith, Arash Mohtashamian, et al. Development and validation of a deep learning algorithm for gleason grading of prostate cancer from biopsy specimens. *JAMA oncology*, 6(9):1372–1380, 2020.

Nikunj Saunshi, Orestis Plevrakis, Sanjeev Arora, Mikhail Khodak, and Hrishikesh Khandeparkar. A theoretical analysis of contrastive unsupervised representation learning. In *International Conference on Machine Learning*, pp. 5628–5637. PMLR, 2019.

Zhuchen Shao, Hao Bian, Yang Chen, Yifeng Wang, Jian Zhang, Xiangyang Ji, et al. Transmil: Transformer based correlated multiple instance learning for whole slide image classification. *Advances in Neural Information Processing Systems*, 34, 2021.

Yash Sharma, Aman Shrivastava, Lubaina Ehsan, Christopher A Moskaluk, Sana Syed, and Donald Brown. Cluster-to-conquer: A framework for end-to-end multi-instance learning for whole slide image classification. In *Medical Imaging with Deep Learning*, pp. 682–698. PMLR, 2021.

Karin Stacke, Jonas Unger, Claes Lundström, and Gabriel Eilertsen. Learning representations with contrastive self-supervised learning for histopathology applications. *arXiv preprint arXiv:2112.05760*, 2021.

Peter Ström, Kimmo Kartasalo, Henrik Olsson, Leslie Solorzano, Brett Delahunt, Daniel M Berney, David G Bostwick, Andrew J Evans, David J Grignon, Peter A Humphrey, et al. Artificial intelligence for diagnosis and grading of prostate cancer in biopsies: a population-based, diagnostic study. *The Lancet Oncology*, 21(2):222–232, 2020.

Yuri Tolkach, Tilmann Dohmgörgen, Marieta Toma, and Glen Kristiansen. High-accuracy prostate cancer pathology using deep learning. *Nature Machine Intelligence*, 2(7):411–418, 2020.

Naofumi Tomita, Behnaz Abdollahi, Jason Wei, Bing Ren, Arief Suriawinata, and Saeed Hassanpour. Attention-based deep neural networks for detection of cancerous and precancerous esophagus tissue on histopathological slides. *JAMA network open*, 2(11):e1914645–e1914645, 2019.

Madeleine Udell, Corinne Horn, Reza Zadeh, Stephen Boyd, et al. Generalized low rank models. *Foundations and Trends® in Machine Learning*, 9(1):1–118, 2016.

Sinong Wang, Belinda Z Li, Madian Khabsa, Han Fang, and Hao Ma. Linformer: Self-attention with linear complexity. *arXiv preprint arXiv:2006.04768*, 2020a.

Yongjun Wang, Baiying Lei, Ahmed Elazab, Ee-Leng Tan, Wei Wang, Fanglin Huang, Xuehao Gong, and Tianfu Wang. Breast cancer image classification via multi-network features and dual-network orthogonal low-rank learning. *IEEE Access*, 8:27779–27792, 2020b.

John Wright and Yi Ma. *High-dimensional data analysis with low-dimensional models: Principles, computation, and applications*. Cambridge University Press, 2022.

Yunyang Xiong, Zhanpeng Zeng, Rudrasis Chakraborty, Mingxing Tan, Glenn Fung, Yin Li, and Vikas Singh. Nyströmformer: A nystöm-based algorithm for approximating self-attention. In *Proceedings of the... AAAI Conference on Artificial Intelligence. AAAI Conference on Artificial Intelligence*, volume 35, pp. 14138. NIH Public Access, 2021.

Hongrun Zhang, Yanda Meng, Yitian Zhao, Yihong Qiao, Xiaoyun Yang, Sarah E Coupland, and Yalin Zheng. Dtfd-mil: Double-tier feature distillation multiple instance learning for histopathology whole slide image classification. In *Proceedings of the IEEE/CVF Conference on Computer Vision and Pattern Recognition*, pp. 18802–18812, 2022.

Yangmuzi Zhang, Zhuolin Jiang, and Larry S Davis. Learning structured low-rank representations for image classification. In *Proceedings of the IEEE conference on computer vision and pattern recognition*, pp. 676–683, 2013.

Xiaowei Zhou, Can Yang, Hongyu Zhao, and Weichuan Yu. Low-rank modeling and its applications in image analysis. *ACM Computing Surveys (CSUR)*, 47(2):1–33, 2014.

A Low-Rank Property of WSI

High-dimensional WSI data bring great challenges to data analysis. But fortunately, the high-dimensional WSI data often lie in low-dimensional subspace, consistent with findings include natural images in computer vision, documents in natural language processingUdell et al. (2016); Zhang et al. (2013); Zhou et al. (2014); Wright & Ma (2022). Pursuing the low-rank property of high-dimensional data is to identify the intrinsic manifold or physical mechanisms from which the data are generated.

Given a bag of feature embedding from a WSI, it can be formulated as a data matrix $\mathbf{X} = [\mathbf{X}_1, \cdots, \mathbf{X}_r]^\top$ where $\mathbf{X}_i$ corresponds to latent class i, r is the total number of latent classes. Ideally, $\mathbf{X}$ can be decomposed into a low-rank component $\mathbf{DB}$ and a sparse error component $\mathbf{E}$, i.e.,

$\mathbf{X} = \mathbf{DB} + \mathbf{E}$ with respect to dictionary, the optimal representation matrix $\mathbf{B}$ for $\mathbf{X}$ should be block-diagonal:

$$\begin{bmatrix} \mathbf{B}_1 & 0 & 0 & 0 \\ 0 & \mathbf{B}_2 & 0 & 0 \\ 0 & 0 & \ddots & 0 \\ 0 & 0 & 0 & \mathbf{B}_r \end{bmatrix} \tag{20}$$

The space matrix $\mathbf{D} = [\mathbf{D}_1, \mathbf{D}_2, ...\mathbf{D}_r]$ contains r sub-space. An example of optimal decomposition for feature embedding is illustrated in Fig. (5). For example, data $\mathbf{X} = [\mathbf{X}_1, \mathbf{X}_2, \mathbf{X}_3]$ contains features from 3 classes, where $\mathbf{X}_1$ contains 3 samples $\boldsymbol{x}_1, \boldsymbol{x}_2, \boldsymbol{x}_3$, $\mathbf{X}_2$ contains 4 samples $\boldsymbol{x}_4, \boldsymbol{x}_5, \boldsymbol{x}_6, \boldsymbol{x}_7$, and $\mathbf{X}_3$ contains 3 samples $\boldsymbol{x}_8, \boldsymbol{x}_9, \boldsymbol{x}_{10}$. $\mathbf{D}$ has 3 sub-space, and each has 2 support items.

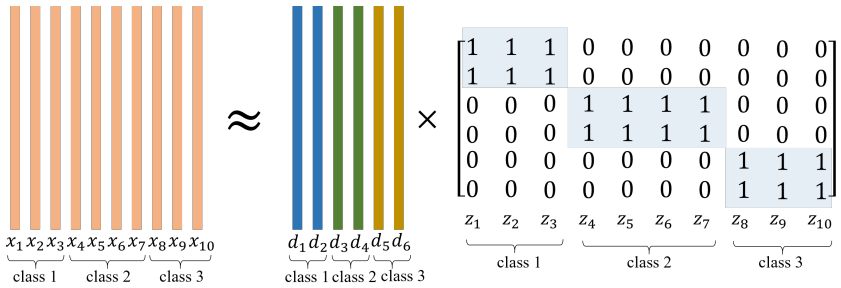

Figure 5: Example of an optimal low-rank decomposition.

Mathematically, the decomposition is achieved by optimizing:

$$\begin{aligned} &\min_{\mathbf{B},\mathbf{E}} \|\mathbf{B}\|_* + \lambda \|\mathbf{E}\|_1 \\ &\text{s.t } \mathbf{X} = \mathbf{DB} + \mathbf{E} \end{aligned} \tag{21}$$

We construct 270 data matrices with CAMLEYON16 training WSIs for low-rank property analysis. The size of data matrix is $\mathbb{R}^{m \times d}$, where m is the bag size of a WSI and d is the fix-dimension of embedding depending on the encoder, e.g., $d = 1024$ for ResNet50 backbone. The low-rank decomposition problem in (21) can be optimized by ADMM algorithm (Alternating Direction Method of Multipliers) Candès et al. (2011); Boyd et al. (2011).

We plot the histogram of the rank of all matrices in Fig. (6. The average rank of ImageNet feature embedding is 349, much smaller than the full-rank 1024. Remarkably, the average rank of self-supervised learning feature BYOLGrill et al. (2020), MoCoChen & He (2021), and the proposed LRC can further reduce to 218, 195, and 181, respectively. As the Table 1 in the main paper shows, the classification performance AUC with the same ILRA-MIL model using ImageNet, BYOL, MoCo, and LRC features is 0.9278, 0.9330, 0.9490, 0.9649, respectively, i.e.:

$$\begin{aligned} \textbf{avg. rank:} \quad & \text{ImageNet} > \text{BYOL} > \text{MoCo} > \text{LRC} \\ \textbf{classification AUC:} \quad & \text{ImageNet} < \text{BYOL} < \text{MoCo} < \text{LRC} \end{aligned} \tag{22}$$

Even without low-rank constraints, BYOL and MoCo tend to produce features with lower ranks than ImageNet. Also, Fig. (6) (d) indicates that the distribution of all WSIs feature embedding is more compact than ImageNet. *This empirical evidence implicitly shows that low-rank features are very likely to be beneficial to WSI representation.*

B Derivation of $\mathcal{L}_{\text{LRC}}$

The derivation of $\mathcal{L}_{\text{LRC}}$ incorporates the contrastive margin into the standard SupCon loss $\mathcal{L}_{\text{SupCon}}$ for positive pair classification.

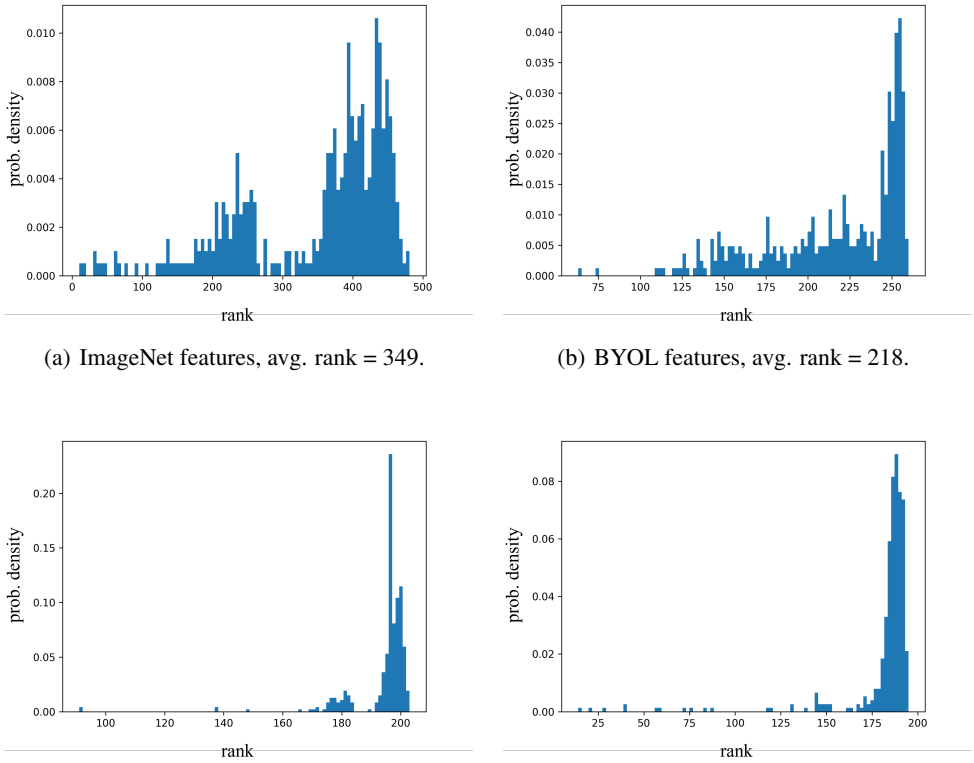

(a) ImageNet features, avg. rank = 349.

(b) BYOL features, avg. rank = 218.

(c) MoCo features, avg. rank =195.

(d) LRC features (proposed), avg. rank=181.

Figure 6: The histogram of the rank of feature embedding. Each sample in the histogram is a data matrix by embedding each patch in the WSI as a feature vector.

Starting from a triplet example with an anchor sample $\boldsymbol{t}_a$, positive sample $\tilde{\boldsymbol{t}}_p$, and negative sample $\tilde{\boldsymbol{t}}_n$. The sigmoid function to identify the positive pairs is:

$$\frac{\exp\left(\mathrm{sim}(\boldsymbol{t}_a, \tilde{\boldsymbol{t}}_p)\right)}{\exp\left(\mathrm{sim}(\boldsymbol{t}_a, \tilde{\boldsymbol{t}}_p)\right) + \exp\left(\mathrm{sim}(\boldsymbol{t}_a, \tilde{\boldsymbol{t}}_n)\right)} \tag{23}$$

The positive pair is correctly classified if:

$$\mathrm{sim}(\boldsymbol{t}_a, \tilde{\boldsymbol{t}}_p) \geq \mathrm{sim}(\boldsymbol{t}_a, \tilde{\boldsymbol{t}}_n) \tag{24}$$

We incorporate the margin constraint into the classification boundary so that the positive pair is correctly classified only if:

$$\mathrm{sim}(\boldsymbol{t}_a, \tilde{\boldsymbol{t}}_p) \geq \mathrm{sim}(\boldsymbol{t}_a, \tilde{\boldsymbol{t}}_n) + \xi. \tag{25}$$

The sigmoid in (23) is modified accordingly:

$$\frac{\exp\left(\mathrm{sim}(\boldsymbol{t}_a, \tilde{\boldsymbol{t}}_p)\right)}{\exp\left(\mathrm{sim}(\boldsymbol{t}_a, \tilde{\boldsymbol{t}}_p)\right) + \exp\left(\mathrm{sim}(\boldsymbol{t}_a, \tilde{\boldsymbol{t}}_n) + \xi\right)} \tag{26}$$

Therefore, the cross-entropy loss to identify the positive is:

$$-\log \frac{\exp\left(\mathrm{sim}(\boldsymbol{t}_a, \tilde{\boldsymbol{t}}_p)\right)}{\exp\left(\mathrm{sim}(\boldsymbol{t}_a, \tilde{\boldsymbol{t}}_p)\right) + \exp\left(\mathrm{sim}(\boldsymbol{t}_a, \tilde{\boldsymbol{t}}_n) + \xi\right)} \tag{27}$$

Given an anchor $\boldsymbol{t}_a$, we get r subspace $C_b(a), b = 1, \cdots, r$ as stated in the low-rank representation Eq. (4). We can intuitively consider that each subspace corresponds to a latent class. We thus would

like to discriminate between different subspace, e.g. $C_1(a)$, $C_r(a)$, which are the most and least distant subspace to anchor t_a.

We extends (27) to $C_1(a)$ positive and $C_r(a)$ negative pairs in a sample batch with SupCon Khosla et al. (2020), giving us:

$$\mathcal{L}_{\text{LRC}} = -\sum_{a=1\cdots N} \frac{1}{|C_1(a)|} \sum_{p\in C_1(a)} \log \frac{\exp\left(\text{sim}(\boldsymbol{t}_a, \tilde{\boldsymbol{t}}_p)\right)}{\sum_{j\in\ \{C_1(a)\cup C_r(a)\}\setminus a} \exp\left(\text{sim}(\boldsymbol{t}_a, \tilde{\boldsymbol{t}}_j) + \xi_j\right)}. \tag{28}$$

where $\xi_j = 0$ if $j \in C_1(a)$, otherwise $\xi_j = \xi$.

C How Sensitive Is the Hyper-Parameter in $\mathcal{L}_{\text{LRC}}$?

Eq. (28) aims to push apart two subspaces. We set the top 5% of instances in a training batch as $C_1(a)$ and the bottom 5% as $C_r(a)$ by default. The percentage of $C_1(a)$ controls the estimated positive samples in a minibatch given anchor $\boldsymbol{t}_a$, and helps strike a balance between the benefits it brings with more true positive samples and the inverse effects of using false positive samples.

Table 4 shows the WSI classification evaluations on CAMELYON16 and TCGA-NSCLC datasets for ILRA-MIL models trained with different choices of $C_1(a)$, ranging from 1% to 10%. The best result is highlighted in **bold** and the second best is underlined. The results show that 5% achieves relatively optimal performance on both datasets. A larger percentage of 10% or a smaller percentage of 1% generally leads to worse performance. We find the sensitivity of the hyperparameter is reduced in the range of 3% to 7%.

Table 4: WSI classification evaluations for models trained with different choices of $C_1(a)$

	CAMELYON16		TCGA-NSCLC	
	Accuracy	AUC	Accuracy	AUC
1%	0.8899 ± 0.0365	0.9260 ± 0.0136	0.8897 ± 0.0207	0.9551 ± 0.0191
3%	$\mathbf{0.9287 \pm 0.0090}$	0.9556 ± 0.0098	0.9205 ± 0.0224	0.9710 ± 0.0185
5%	0.9218 ± 0.0113	$\mathbf{0.9649 \pm 0.0844}$	$\mathbf{0.9213 \pm 0.0173}$	0.9763 ± 0.0149
7%	0.9084 ± 0.0215	0.9521 ± 0.0095	0.9200 ± 0.0204	$\mathbf{0.9780 \pm 0.0234}$
10%	0.8884 ± 0.0105	0.9137 ± 0.0139	0.9113 ± 0.0197	0.9663 ± 0.0188

D Training Details

The training data splits are described in Section E. For each dataset, we use the same training data to first develop a self-supervised learning model to conduct local feature embedding and then train MIL models to implement global feature aggregation for classification.

One should pay attention not to exposing test datasets for the development of a feature embedding model, although no labels are used. For example, if the test set of CAMELYON16 is used by MoCo-v3 for feature embedding pretraining, we can achieve **0.9885 AUC** classification performance on the test set with CLAM-MB. This exceptionally high performance is caused by data leakage.

D.1 Self-Supervised Training Details

We train self-supervised learning models to conduct local feature embedding. We closely follow MoCo-V3 Chen et al. (2020c) and use the same training hyper-parameters. For all methods, we use an initial learning rate of $1.5e^{-4}$. We use AdamW as the optimizer and adopt a learning rate warmup for 20 epochs to alleviate instability. Each model is optimized on 16 Nvidia V100 GPUs with a cosine learning rate decay schedule and a mini-batch size of 4096. We train for 200 epochs for CAMELYON16, TCGA-NSCLC, and PANDA.

D.2 MIL TRAINING DETAILS

MIL models, including baseline and ours, are trained on a single Nvidia V100 GPU. They are optimized end-to-end with Adam optimizer with a batch size of 1 and a learning rate of $1e^{-4}$ for 200 epochs. The Adam optimizer has parameters $\beta_1 = 0.9$, $\beta_2 = 0.95$, and $\epsilon = 1e^{-8}$.

E DATASET

Each WSI is cropped into a series of 224×224 non-overlapping patches using a binary mask for the tissue regions which is computed based on thresholding the saturation channel of the image.

CAMELYON16[1] is a public dataset for metastasis detection in breast cancer (2-level classification), including 270 training sets and 130 test sets. A total of about 1.5 million patches at $\times 10$ magnification are obtained after prep-process.

TCGA-NSCLC[2] includes two subtype projects (2-level classification), i.e., Lung Squamous Cell Carcinoma (TGCA-LUSC) and Lung Adenocarcinoma (TCGA-LUAD), for a total of 993 diagnostic WSIs, including 507 LUAD slides from 444 cases and 486 LUSC slides from 452 cases. We obtain 3.4 million patches in total at $\times 10$ magnification .

PANDA[3] is the largest prostate biopsy public dataset to date Bulten et al. (2022). We only use slides with pure and unequivocal patterns (from 0+0, 3+3, 4+4, or 5+5 slides) where the inter-observer variability was normally low Tolkach et al. (2020); Bulten et al. (2022); Ström et al. (2020), making it a 4-level classification problem. We use 4369 slides (1924 slide of 0+0, 1813 slides of 3+3, 466 slides of 4+4, 166 slides of 5+5) from Karolinska Institute for training , and 2591 slides (962 slide of 0+0, 852 slides of 3+3, 660 slides of 4+4, 111 slides of 5+5) from Radboud University for testing. A total of 1.1 million patches at $\times 10$ magnification are obtained.

F CLASSIFICATION RESULTS ON BENCHMARKS

The following Table 5 and Table 6 are extensions of Table 1 in the main paper with the standard deviation. Each experiment is conducted for 5 runs with respect to different random startup seeds on the same data splits.

Table 5: Results on Benchmarks CAMELYON16 and TCGA-NSCLC.

	CAMELYON16		TCGA-NSCLC	
	Accuracy	AUC	Accuracy	AUC
Mean-pooling	0.6511 ± 0.015	0.6755 ± 0.0415	0.7282 ± 0.0181	0.8551 ± 0.0429
Max-pooling	0.7674 ± 0.004	0.8169 ± 0.0254	0.8593 ± 0.0451	0.9263 ± 0.0585
ABMIL	0.8527 ± 0.0252	0.8503 ± 0.0293	0.8384 ± 0.0260	0.9205 ± 0.0259
MIL-RNN	0.8449 ± 0.0257	0.8580 ± 0.0314	0.8619 ± 0.0404	0.9107 ± 0.0430
CLAM-SB	0.8682 ± 0.0133	0.8709 ± 0.0135	0.8632 ± 0.0267	0.9307 ± 0.0162
CLAM-MB	0.8604 ± 0.0215	0.8779 ± 0.0193	0.8492 ± 0.0294	0.9377 ± 0.0139
DSMIL	0.8759 ± 0.0231	0.8944 ± 0.0184	0.8690 ± 0.0277	0.9439 ± 0.0215
DSMIL + SimCLR	0.8867 ± 0.0201	0.9175 ± 0.0139	0.9048 ± 0.0225	0.9551 ± 0.0187
TransMIL	0.8449 ± 0.0381	0.8669 ± 0.0273	0.8565 ± 0.0178	0.9303 ± 0.0154
DTFD-MIL	0.9010 ± 0.0341	0.9401 ± 0.0272	0.8941 ± 0.0331	0.9612 ± 0.0223
ILRA-MIL	$\mathbf{0.8992 \pm 0.0184}$	$\mathbf{0.9278 \pm 0.0121}$	$\mathbf{0.9004 \pm 0.0218}$	$\mathbf{0.9592 \pm 0.0176}$
ILRA-MIL + LRC	$\mathbf{0.9218 \pm 0.0113}$	$\mathbf{0.9649 \pm 0.0096}$	$\mathbf{0.9213 \pm 0.0173}$	$\mathbf{0.9763 \pm 0.0149}$

G HEATMAPS

Figure 7 shows 4 diverse examples on the CAMLEYON16 test set. In the "raw image" column, the tumor area is delineated by the blue line. In the "CLAM" and "CLAM+LRC" columns, brighter red

[1] https://camelyon16.grand-challenge.org/Data/

[2] https://portal.gdc.cancer.gov/

[3] https://www.kaggle.com/competitions/prostate-cancer-grade-assessment/data

Table 6: Results on PANDA test set.

	PANDA	
	Accuracy	kappa
Mean-pooling	0.5691 ± 0.0493	0.4422 ± 0.0248
Max-pooling	0.6100 ± 0.0255	0.5830 ± 0.0460
ABMIL	0.6834 ± 0.0177	0.5998 ± 0.0155
MIL-RNN	NA	NA
CLAM-SB	0.6648 ± 0.0368	0.5782 ± 0.0182
CLAM-MB	0.6760 ± 0.0441	0.6067 ± 0.0161
DSMIL	0.6737 ± 0.0468	0.5562 ± 0.0427
DSMIL + SimCLR	0.7017 ± 0.0530	0.5837 ± 0.0231
TransMIL	0.6720 ± 0.0434	0.5638 ± 0.0135
DTFD-MIL	0.6573 ± 0.0218	0.5437 ± 0.0193
ILRA-MIL	$\mathbf{0.7094 \pm 0.0309}$	$\mathbf{0.6236 \pm 0.0143}$
ILRA-MIL + LRC	$\mathbf{0.7287 \pm 0.0210}$	$\mathbf{0.6562 \pm 0.0244}$

indicates that the higher attention score is the tumor at the corresponding location. ”CLAM” is the original CLAM-SB method Lu et al. (2021c) whereas ”CLAM+LRC” incorporates CLAM-SB with our proposed LRC feature embedding method.

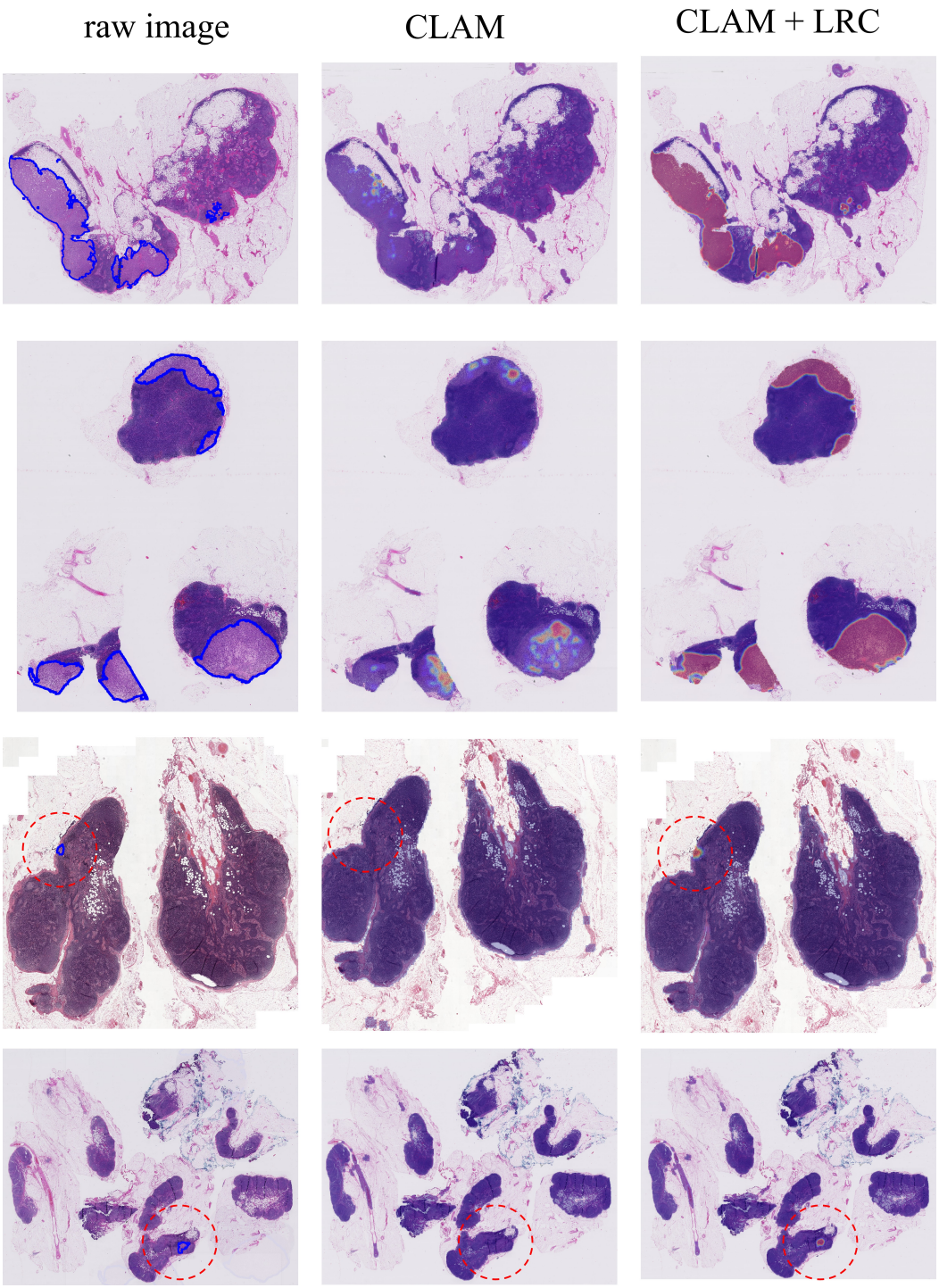

Figure 7: Four examples of high-resolution heatmaps of the CAMELYON16 test set, namely test_016, test_073, test_117, and test_092 from the top row to the bottom row. We compare the heatmap of CLAM in the second column with our proposed LRC method in the third column. Our method is more consistent with the ground truth annotations, indicating superior performance.